

# Spatial Coupling between Lunar Surface Mineral Abundance and Morphological Features Based on Visible-Near Infrared Remote Sensing

Jiao Leilei<sup>1</sup>, Xu Yusheng<sup>1,2</sup>, Huang Rong<sup>1,2</sup>, Liu Shijie<sup>1,2\*</sup>, Tang Panli<sup>1,2</sup>, Wang Chao<sup>1,2</sup>, Feng Yongjiu<sup>1,2</sup>, Tong Xiaohua<sup>1,2</sup>

(1. College of Surveying and Geo-Informatics, Tongji University, Shanghai 200092, China;  
2. Shanghai Key Laboratory of Space Surveying, Remote Sensing and Spatial Exploration, Tongji University, Shanghai 200092, China)

**Abstract:** The spatial distribution of lunar surface minerals provides essential constraints on magmatic activity, material differentiation, and subsequent impact modification, and is fundamental for reconstructing the Moon's evolutionary history from remote-sensing observations. In this study, visible - near infrared (415 - 950 nm) mineral abundance products derived from the Multiband Imager (MI) onboard SELENE (Kaguya) were integrated with digital elevation model (DEM) - derived topographic parameters to conduct a quantitative, unified-scale spatial analysis of mineral - geomorphology relationships within lunar mare units. Representative large-scale impact structures and mare basins, including the Von Kármán crater and Mare Crisium, were selected as study areas to characterize the spatial correlation between near-infrared-sensitive mineral abundances and geomorphological features across different geological units. The results reveal significant regional-scale spatial clustering of mineral abundances and topographic parameters, along with pronounced spatial non-stationarity across varying geological and structural settings. These spatial patterns reflect the coupled long-term effects of magmatic activity, subsequent impact modification, and their interaction with pre-existing topography, thereby establishing a quantitative framework for lunar surface geological interpretation and evolutionary analysis using remote-sensing data.

**Key words:** Lunar mineral, morphological features, bivariate spatial autocorrelation, geographically weighted regression(GWR)

## Introduction

The Moon, Earth's only natural satellite, preserves records of fundamental geological processes of the early Solar System in its surface composition and geomorphology, including crustal differentiation, magmatic activity, and large-scale impact events<sup>[1-2]</sup>. Impact cratering is the dominant process governing surface evolution on airless planetary bodies. Transient high-energy impacts rapidly modify local topography and generate complex craters and multi-ring basins. Associated excavation, ejecta redistribution, and impact melting expose the spatial heterogeneity of lunar surface materials<sup>[3]</sup>. Repeated impact events have further reworked the lunar surface and redistributed crustal materials through time<sup>[3-5]</sup>.

Large impact basins and their surroundings are key targets for understanding lunar impact processes and crustal evolution. Basin interiors exhibit multiple concentric ring structures, whereas extensive ejecta blankets result from bedrock fragmentation, material mixing, and

long-range ejecta transport. These geomorphic features are commonly associated with heterogeneous mineral exposures and therefore provide constraints on the Moon's early thermal and geological evolution<sup>[6]</sup>.

Recent lunar missions have acquired extensive high-resolution remote sensing datasets. Orbital observations, in situ measurements, and sample return analyses enable detailed characterization of lunar geological evolution and surface morphology. Mineral abundance products derived from imaging spectroscopy and thermal infrared remote sensing constrain the spatial distributions of major minerals, including pyroxene, plagioclase, olivine, and ilmenite<sup>[7-9]</sup>. Digital elevation models (DEMs) generated from laser altimetry and stereo imagery provide topographic parameters such as elevation, slope, curvature, and relief, which quantitatively describe geomorphic responses to geological processes<sup>[10]</sup>. These datasets have been widely used to map volcanic units, interpret ejecta composition, and infer crustal structure<sup>[3,5,10]</sup>. However,

Received date: 2026-02-10, accepted date: 2026-04-16

收稿日期: 2026-02-10, 录用日期: 2026-04-16

Foundation items: Supported by the National Key Research and Development Program of China (2022YFF0504100); the National Natural Science Foundation of China (42221002, 42201478); and the Shanghai Basic Research Pilot Program (22TQ1400300).

\*Corresponding author: E-mail: liusjtj@tongji.edu.cn

quantitative evaluation of how topographic variability influences mineralogical patterns remains limited, especially at local to regional scales.

Lunar surface mineralogy and its spatial distribution are core objectives of planetary exploration<sup>[11-12]</sup>. The dominant lunar mineral phases include plagioclase, pyroxene, and olivine. Plagioclase constitutes the primary component of the anorthositic highland crust<sup>[1]</sup>, whereas mare basalts commonly contain ilmenite-rich opaque phases. Variations in ilmenite abundance constrain basaltic magma source properties and magmatic differentiation processes<sup>[13]</sup>. Previous studies have also shown that slope and terrain geometry can affect spectral retrievals, complicating interpretations of mineral distributions when topographic effects are not considered. Plagioclase-rich highland materials tend to be associated with steeper crater walls and slopes, whereas pyroxene- and ilmenite-rich mare lavas are generally observed in flatter plains and gently sloping volcanic landforms<sup>[14-17, 19-20]</sup>. Analyses of Chang'e-6 returned samples and related remote sensing studies have suggested that ejecta emplacement and redeposition may produce localized mineral enrichment around large impact craters<sup>[12]</sup>. Although mineral abundance and topography have both been widely investigated, they have usually been analyzed separately, and their relationship has rarely been quantified in an integrated spatial framework<sup>[17-18]</sup>.

Despite substantial progress in mineral inversion and geomorphic interpretation, limitations remain. Previous studies primarily focused on single-factor analyses, deriving mineral abundance from M<sup>3</sup><sup>[17]</sup> and Diviner<sup>[18]</sup> data and interpreting geological structures using topography. Most relied on qualitative comparisons or simple correlations and lacked quantitative characterization of spatial co-variation between mineral abundance and geomorphic parameters<sup>[19-20]</sup>. Moreover, analyses were commonly restricted to individual landing sites or representative craters, with few regional-scale comparisons across different geological units<sup>[21-22]</sup>.

Spatially explicit methods are well suited to addressing these limitations because lunar surface processes are strongly heterogeneous, spatially non-stationary, and scale dependent<sup>[3-6]</sup>. Recent studies have demonstrated the applicability of spatial statistical approaches to lunar remote sensing analysis. For example, Feng et al.<sup>[23]</sup> used bivariate spatial autocorrelation and geographically weighted regression to investigate relationships between mineral abundance and brightness temperature across the Moon.

To address these limitations, this study integrates Kaguya Multiband Imager mineral products with co-registered DEMs and applies Global Moran's I, Local Moran's I, and geographically weighted regression to quantify mineral - topography relationships. The analysis focuses on lunar mare units, with particular emphasis on the Von Kármán impact structure and Mare Crisium, to compare spatial coupling patterns under different geological settings.

This study aims to quantify the relationships be-

tween major mineral abundances and topographic parameters in lunar mare units at both global and local scales, with particular emphasis on the Von Kármán impact structure and Mare Crisium. This study integrates spatial autocorrelation metrics with geographically weighted regression to provide a spatially explicit framework for analyzing how local variations in lunar topography influence the distribution of key minerals, enabling quantitative assessment of coupled compositional and geomorphic heterogeneity. The results not only improve understanding of how topography influences mineral distribution under different geological settings, but also provide useful support for lunar geological interpretation, landing-site assessment, and future exploration planning.

## 1 Data and Methods

### 1.1 Data and preprocessing

The datasets used in this study include a lunar digital elevation model (DEM) for topographic parameter extraction and multispectral remote sensing data from the SELENE (Kaguya) Multiband Imager (MI) for mineralogical analysis.

Topographic data are derived from laser altimeter observations acquired by the Chang'e-1 mission. An interpolated global lunar DEM with a spatial resolution of ~500 m and a vertical accuracy better than 50 m is used as the primary topographic dataset. As an active remote sensing technique, laser altimetry is insensitive to solar illumination and provides continuous, quantitatively reliable measurements of lunar surface topography, forming a sound basis for analyzing the relationships between mineral distribution and geomorphic features. To characterize lunar surface morphology, key topographic parameters—including elevation, slope, aspect, curvature, shade, roughness and relief—are derived from the DEM using terrain analysis and spatial differential operations.

Mineralogical data are obtained from mineral abundance products derived from the Multiband Imager (MI) onboard the SELENE (Kaguya) lunar mission. The MI consists of five visible bands (430 - 850 nm) with a spatial resolution of 20 m and four near-infrared bands (960 - 1600 nm) with a spatial resolution of 62 m<sup>[24-25]</sup>. Mineral abundance products are generated based on visible - near-infrared multispectral reflectance characteristics using endmember matching and spectral unmixing approaches, and effectively characterize the spatial distributions of major lunar rock-forming minerals. In this study, four representative minerals—clinopyroxene, orthopyroxene, plagioclase, and olivine—are selected for analysis. These minerals represent key mineral endmembers of mare basaltic units and anorthositic highland units and provide important constraints on lunar crustal composition, magmatic differentiation processes, and the provenance of impact-exposed materials.

The mineral abundance products used in this study were derived from the SELENE/Kaguya MI MAP\_02 processing level data, mosaicked and distributed by USGS at 59 m per pixel resolution<sup>[26-27]</sup>. To ensure spatial consistency with the Chang'e-1 DEM (~500 m resolution),

the MI data were resampled to 500 m using bilinear interpolation. This upscaling (approximately 8:1) aggregates ~64 native pixels into each resampled cell, effectively smoothing local heterogeneity while preserving regional-scale mineral distribution patterns. The 500 m resolution is appropriate for analyzing the relationships between mineral distribution and geomorphology in the large mare basins and impact structures, which is the primary objective of this study.

To ensure spatial consistency in multisource data analysis, MI mineral abundance products are resampled to a spatial resolution of 500 m to match the DEM. All datasets are further subjected to coordinate system unification and spatial coregistration prior to subsequent analysis.

## 1.2 Study area

The study areas include the Mare Crisium Basin on the lunar nearside and the Von Kármán impact crater located in the northeastern portion of the South Pole - Aitken (SPA) basin on the lunar farside (As show in Figure 1).

The Mare Crisium Basin is situated in the eastern region of the lunar nearside. Formed during the Nectarian period, it has a diameter of approximately 1000 km, with its center at  $17^{\circ}\text{N}$ ,  $59.1^{\circ}\text{E}$ <sup>[28]</sup>. The basin interior is infilled by mare basaltic lava flows, whereas the basin rim exhibits annular structural units composed of plagioclase-rich highland crustal material. Basalts with varying titanium contents in the Crisium region display a heterogeneous spatial distribution, reflecting multiple episodes of magmatic activity and material differentiation, and the regional topography has been substantially modified by large impact events.

The South Pole - Aitken (SPA) Basin on the lunar farside has a diameter of approximately 2500 km and formed as a result of a major impact event at ~3.9 Ga, making it one of the largest, deepest, and oldest impact basins on the Moon<sup>[29]</sup>. The Von Kármán impact crater is located in the northwestern sector of the SPA Basin, with a central coordinate of  $44.5^{\circ}\text{S}$ ,  $176.25^{\circ}\text{E}$ . The crater floor is relatively flat and has been infilled by later basaltic lava flows<sup>[30]</sup>. The material composition and geological

age of the crater are representative of impact-modified and mare-filled units within the SPA Basin, providing important constraints on early lunar impact evolution.

## 1.3 Methods

This study integrates mineral abundance products derived from visible - near-infrared observations of the SELENE (Kaguya) Multiband Imager (MI) with topographic parameters, applying bivariate Moran's  $I$  and geographically weighted regression (GWR) to construct a spatial-statistics-based workflow for analyzing the coupling between lunar surface mineralogy and geomorphic features at both global and local scales (Figure 2).

The MI mineral abundance data and the digital elevation model (DEM) were first preprocessed to ensure spatial consistency. This included unifying the coordinate system and resampling both datasets to a common spatial resolution. Topographic parameters relevant to surface geomorphology, such as elevation, slope, and relief were then derived from the DEM.

To investigate the coupling between near-infrared - sensitive mineral abundances and topographic parameters, bivariate spatial autocorrelation (Bivariate Moran's  $I$ ) was first used to assess overall spatial dependence. Local spatial patterns and clustering of mineral - geomorphology relationships were then examined using Bivariate Local Indicators of Spatial Association (Bi-LISA). Geographically weighted regression (GWR) was subsequently applied to quantify spatially non-stationary relationships across different geological units. The resulting maps of regression coefficients reveal spatial heterogeneity in mineral - geomorphology coupling, providing quantitative constraints for interpreting mineral distribution mechanisms within impact basins and mare units.

### 1.3.1 Bivariate Spatial Autocorrelation

The distribution of minerals on the lunar surface exhibits significant spatial clustering rather than random patterns, showing spatial structural characteristics such as spatial autocorrelation and spatial dependence<sup>[23]</sup>. Unlike conventional statistical analyses, which do not consider spatial proximity and therefore may not capture spatial associations between two variable sets, spatial autocorrelation quantitatively assesses correlation structures

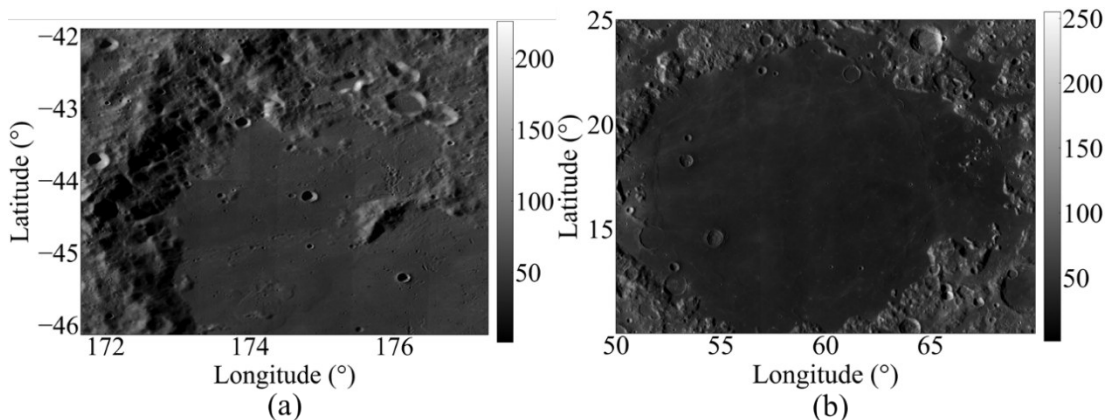


Fig. 1 Map of the study area: (a) Von Kármán; (b) Mare Crisium Basin  
图1 研究区示意图: (a)冯·卡门撞击坑; (b)危海盆地

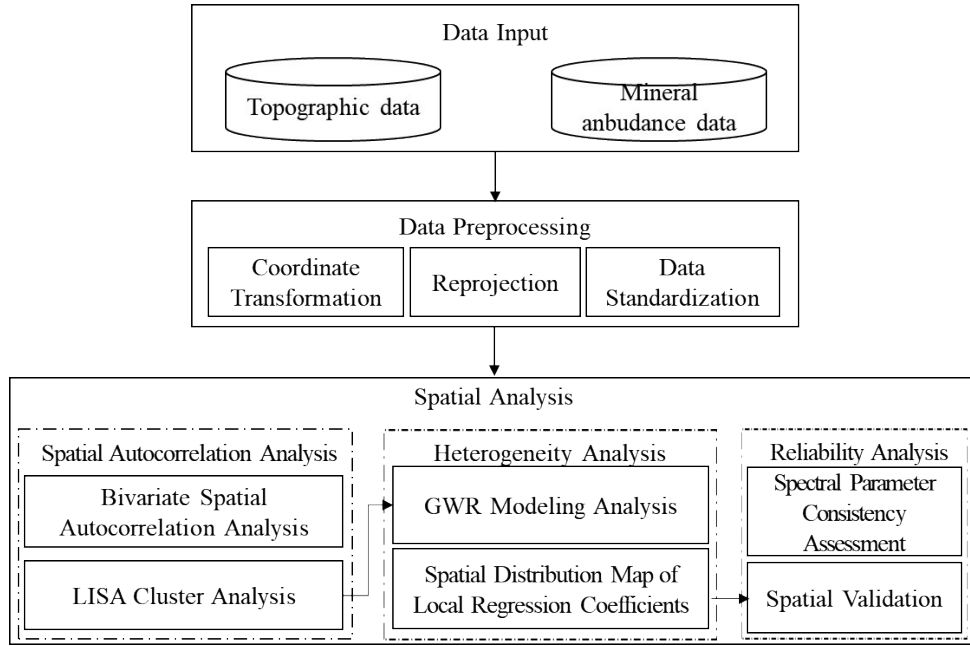


Fig. 2 Workflow of spatial coupling analysis between mineral abundance and geomorphological features on the lunar surface  
图2 月表矿物与形貌特征空间分析流程

among spatial units through a spatial weight matrix. Moran's  $I$  quantifies the degree of dependence between geographic variables at a given scale and serves as an indicator for the spatial association between lunar surface morphological features and mineral abundances<sup>[31]</sup>.

Bivariate Moran's  $I$  characterizes the joint spatial-neighborhood association between a mineral abundance variable  $x$  and a topographic parameter variable  $y$  within a spatial unit<sup>[32]</sup>, providing a means to investigate spatial relationships between morphology and mineral distribution. It is expressed as:

$$\text{Moran's } I = \frac{\sum_i \left( \sum_j \omega_{ij} z_i^m \times z_j^n \right)}{\sum_i (z_i^p)^2}, \quad (1)$$

where  $x_i$  is the mineral abundance value at grid cell  $i$ ,  $y_j$  represents the topographic parameter value at the neighboring cell  $j$ ,  $\bar{x}$  and  $\bar{y}$  indicate the sample means of mineral abundance and topographic parameters within the study area, respectively, calculated as the arithmetic average of all valid grid cells.  $z_i^m$  and  $z_j^n$  denote the standardized values of mineral abundance and topographic parameters.  $\omega_{ij}$  is an element of the spatial weight matrix, with  $\omega_{ij} > 0$  if cells  $i$  and  $j$  are neighbors and  $\omega_{ij} = 0$  otherwise. In this study, the spatial weight matrix is constructed based on contiguity in a regular grid framework and normalized to ensure comparability across locations. Moran's  $I$  ranges between  $[-1, 1]$ . A value greater than 0 indicates positive spatial clustering between mineral abundance and topographic parameters; a value close to 0 suggests near-random spatial distribution; and a value less than 0 reflects spatial dispersion between the variables.

### 1.3.2 Bivariate Local Spatial Autocorrelation

Building on global spatial autocorrelation, bivariate local spatial autocorrelation characterizes clustering patterns at a local scale. To quantify spatial relationships between the mineral grid cells, a row standardized spatial weight matrix  $W$  was constructed using the Queen contiguity criterion, where neighboring cells sharing either a common edge or a common vertex were assigned weights  $\omega_{ij} = \frac{1}{k_i}$ , with  $k_i$  denoting the number of neighbors for cell  $i$ , and non-neighbors received zero weights. This criterion effectively captures spatial continuity by considering all adjacent neighbors, including those touching at vertices, which is particularly suitable for irregular geologic units on planetary surfaces. By calculating the local Moran's  $I$  for each grid cell, spatial aggregation patterns between mineral abundance and topography can be identified. The local Moran's  $I$  is defined as:

$$\text{Bi-LISA} = \frac{\sum_j \omega_{ij} z_i z_j}{\sum_i (z_i^2)}. \quad (2)$$

Based on the combination of standardized variables, local spatial associations are classified into four types: high-high (HH), high-low (HL), low-low (LL), and low-high (LH). HH and LL patterns reflect local synergistic clustering of mineral abundance and topographic parameters, often governed by the same geological processes. In contrast, HL and LH patterns indicate spatially inconsistent variations between mineral abundance and topography, typically occurring at crater rims, mare-highland transition zones, or regions influenced by multi-phase material superposition.

### 1.3.3 Geographically Weighted Regression Mod-

el

Spatial autocorrelation measures similarity in mineral – topography relationships but does not account for potential spatial non-stationarity. To address this, geographically weighted regression (GWR) is employed. GWR incorporates spatial location into the regression, allowing coefficients to vary by location and estimating local regression parameters for each spatial unit. The model relates mineral abundance (dependent variable) to topographic parameters (independent variables) as:

$$y_i = \beta_0(m_i, n_i) + \sum_{k=1}^p \beta_k(m_i, n_i) x_{ik} + \varepsilon_i, \quad (3)$$

where  $y_i$  is the mineral abundance at location  $i$ ,  $x_{ik}$  ( $k = 1, 2 \dots p$ ) denotes the  $k$ -th topographic parameter at location  $i$ ,  $(m_i, n_i)$  are the spatial coordinates of the regression point,  $\beta_0(m_i, n_i)$  is the location-specific intercept, and  $\beta_k(m_i, n_i)$  ( $k = 1, 2 \dots p$ ) are spatially varying local regression coefficients, and  $\varepsilon_i$  represents the random error term (residual) at location  $i$ , which is assumed to be independently and identically distributed with a mean of zero. Considering the compositional and tectonic differences between mare and highland units, the study area is subdivided according to a lunar geological map, and local regression is performed within geologically homogeneous units.

To visualize the spatial patterns of mineral abundance and regression coefficients, the Getis-Ord ( $G_i^*$ ) statistic is applied to the spatially continuous GWR results. High- and low-value clusters reveal zones of mineral enrichment and areas where the mineral – topography coupling is relatively strong or weak, thereby characterizing the spatial heterogeneity in the relationships between minerals and topographic features. The statistic is defined as:

$$G_i^* = \frac{\sum_{n=1}^p w_{in} a_n - \bar{a} \sum_{n=1}^p w_{in}}{\sqrt{\frac{p \sum_{n=1}^p \omega_{in}^2 - \left( \sum_{n=1}^p \omega_{in} \right)^2}{p-1}}}. \quad (4)$$

Here, the  $G_i^*$  identifies local clustering of spatial variables, where  $p$  refers to the number of neighboring geomorphological features considered in the computation,  $a_n$  represents the mineral abundance value (or the GWR regression coefficient) at location  $n$ ,  $\bar{a}$  denotes the corresponding global mean. By statistically assessing the spatial deviation of  $a_n$  relative to  $\bar{a}$ , the  $G_i^*$  enables the identification of significant high-value clusters ("hot spots") and low-value clusters ("cold spots") in mineral abundance and GWR regression coefficients. This approach effectively characterizes the spatial heterogeneity of mineral distribution patterns and the localized variability in the strength of association between mineral abundance and geomorphological parameters, thereby providing a quantitative basis for analyzing the spatial differentiation structure of lunar surface minerals.

## 2 Results

### 2.1 Spatial relationships between geomorphic features and plagioclase abundance

Plagioclase, as a major component of the lunar highland crust, exhibits spatial distributions that respond to the underlying geomorphic context. Using bivariate Moran's  $I$  and significance tests, the spatial associations between plagioclase abundance and topographic parameters were quantitatively assessed for the Von Kármán crater and the Mare Crisium Basin.

At the Von Kármán crater (Figure 3(a)), plagioclase abundance shows the strongest bivariate Moran's  $I$  with aspect, with Moran's  $I = 0.052$  and  $p < 0.01$ , indicating a statistically significant but weak spatial association. Slope shows a weak positive spatial association (Moran's  $I = 0.011$ ,  $p < 0.01$ ). In contrast, bivariate Moran's  $I$  values for other topographic parameters, including roughness, shade, and elevation, are close to zero but statistically significant ( $p < 0.05$ ), indicating weak but non-random spatial structure, whereas curvature and relief are not statistically significant ( $p > 0.05$ ), suggesting a lack of clear spatial coupling between these parameters and plagioclase abundance in this study area.

In the Mare Crisium Basin (Figure 3(b)), roughness and shade exhibit significant positive spatial associations with plagioclase abundance (Moran's  $I = 0.112$ ,  $p < 0.001$ ; Moran's  $I = 0.108$ ,  $p < 0.01$ , respectively). Slope shows a weak but statistically significant association (Moran's  $I = 0.008$ ,  $p < 0.01$ ), whereas elevation does not exhibit a significant spatial relationship (Moran's  $I = 0.050$ ,  $p = 0.40$ ). Aspect, curvature, and relief are also not statistically significant ( $p > 0.05$ ). Accordingly, roughness and shade represent the primary topographic variables associated with the spatial distribution of plagioclase abundance in this basin.

These contrasting relationships indicate spatial non-stationarity in the association between plagioclase abundance and topography, reflecting the influence of differing geomorphic settings in the two regions.

### 2.2 Local spatial associations between geomorphic features and plagioclase abundance

Bivariate Local Indicators of Spatial Association (BILISA) results (Tables 1 and 2) show clear spatial clustering of plagioclase abundance with multiple topographic parameters in both the Von Kármán crater and the Mare Crisium Basin. However, clustering patterns differ significantly between geological units, indicating spatial non-stationarity in the mineral – topography relationships.

At the Von Kármán crater (Table 1), clustering with elevation is most pronounced. High – high (HH) and low – low (LL) clusters occupy a large proportion of the area. High-plagioclase units generally correspond to regions with higher elevation, slope, and relief, whereas low-plagioclase units occur in areas with lower relief and lower slopes. This pattern indicates a stable spatial response of plagioclase abundance to topographic heterogeneity within the crater. In contrast, aspect shows rela-

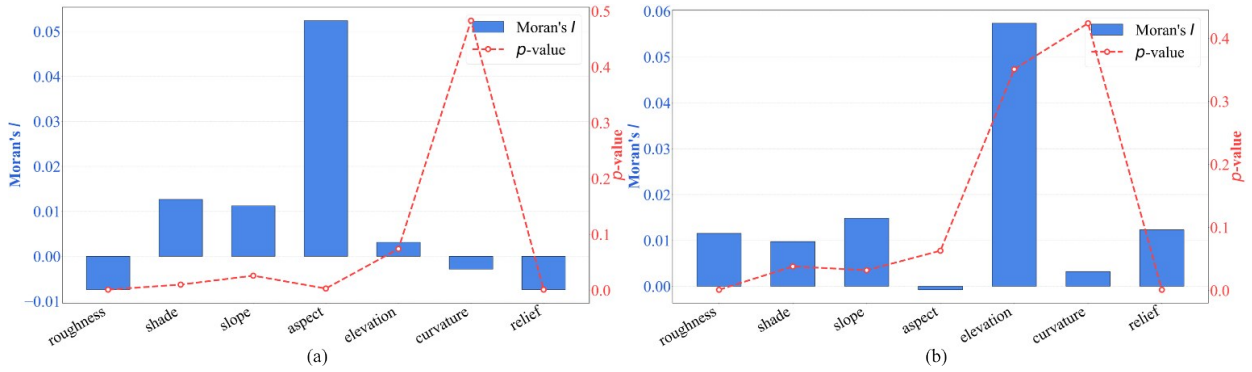


Fig. 3 Spatial associations between geomorphological features and plagioclase abundance: (a) Von Kármán; (b) Mare Crisium Basin  
图3 形貌特征与斜长石丰度的空间关系: (a)冯·卡门撞击坑; (b)危海盆地

tively weak spatial clustering with plagioclase abundance.

In the Mare Crisium Basin (Table 2), elevation also exhibits significant spatial clustering with plagioclase abundance. High - high (HH) clusters account for 29.02% of the area, with an average abundance of 0.7011, indicating that high-plagioclase units are concentrated in higher-elevation regions. Low - low (LL) clusters, although the largest proportion (42.19%), have an average abundance of only 0.4595, reflecting generally lower plagioclase abundance in low-elevation areas. In addition to elevation, roughness and relief also show relatively high proportions within HH clusters, indicating that plagioclase-rich regions tend to co-occur with areas of stronger relief.

The differences in spatial clustering patterns between the two study areas correspond closely to their respective mare and highland geological contexts, indicating that under similar topographic conditions, plagioclase abundance still exhibits regional variations in spatial aggregation<sup>[33]</sup>.

### 2.3 Local responses of minerals to geomorphic features

At the study-area scale, geographically weighted regression (GWR) models were constructed to quantify the spatially non-stationary relationships between mineral abundances and topographic parameters. Lunar geologic maps were then incorporated to delineate geological units, providing a spatially constrained framework for analysis. This approach enables statistical characterization of continuous spatial variations in plagioclase abundance under mare and highland backgrounds, as well as local response patterns of mineral - topography coupling. The  $G_i^*$  statistic was further applied to visualize the spatial clustering of GWR regression coefficients.

Using multispectral remote sensing imagery and digital elevation data, a GWR model was established for the Von Kármán crater to characterize spatially non-stationary relationships between plagioclase abundance and topographic factors including elevation, slope, and curvature. By integrating lunar geologic maps as a spatial constraint, the coupling mechanisms between mineral abundances and topographic parameters at local scales were further revealed.

Table 1 Summary statistics of topographic features and plagioclase abundance for Bi-LISA in Von Kármán

表1 冯卡门撞击坑斜长石丰度与形貌特征的双变量LISA统计结果

Features	Cluster	Percent (%)	Min	Max	Mean	SD
elevation	HH	18.96	0.6	0.81	0.6497	0.0271
	LH	16.7	0.39	0.64	0.5824	0.0325
	LL	30.75	0.3	0.64	0.5831	0.0331
	HL	33.59	0.6	0.81	0.6501	0.0252
slope	HH	31.89	0.6	0.81	0.6493	0.026
	LH	28.8	0.3	0.64	0.5833	0.0326
	LL	18.66	0.36	0.64	0.5822	0.0333
	HL	20.65	0.6	0.81	0.6509	0.0258
aspect	HH	25.93	0.6	0.81	0.6509	0.0267
	LH	22.42	0.3	0.64	0.5838	0.0325
	LL	25.03	0.36	0.64	0.582	0.0332
	HL	26.61	0.6	0.81	0.6489	0.0251
roughness	HH	19.69	0.6	0.81	0.6493	0.0259
	LH	17.77	0.39	0.64	0.5828	0.0326
	LL	29.68	0.3	0.64	0.5829	0.0331
	HL	32.68	0.6	0.81	0.6503	0.026
relief	HH	19.58	0.6	0.81	0.6492	0.0258
	LH	17.72	0.39	0.64	0.5828	0.0326
	LL	29.73	0.3	0.64	0.5829	0.0331
	HL	32.97	0.6	0.81	0.6504	0.026
shde	HH	34.04	0.6	0.81	0.6498	0.0262
	LH	30.85	0.38	0.64	0.5829	0.0327
	LL	16.6	0.3	0.64	0.5827	0.0333
	HL	18.51	0.6	0.8	0.6501	0.0254
curvature	HH	25.71	0.6	0.81	0.6501	0.0259
	LH	23.46	0.3	0.64	0.5826	0.033
	LL	23.99	0.36	0.64	0.5831	0.0328
	HL	26.84	0.6	0.81	0.6498	0.0259

Figure 4 presents the comprehensive remote sensing and geostatistical analysis results for the Von Kármán crater. Figure 4(a) and Figure 4(b) display the WAC image and DEM, respectively, providing the geomorpho-

**Table 2 Summary statistics of topographic features and plagioclase abundance for Bi-LISA in Mare Crisium basin****表 2 危海盆地斜长石丰度与形貌特征的双变量 LISA 统计结果**

Features	Cluster	Percent (%)	Min	Max	Mean	SD
elevation	HH	29.02	0.3627	0.9848	0.7011	0.1626
	LH	10.43	0	0.7832	0.4483	0.1307
	LL	42.19	0	0.7832	0.4595	0.1031
	HL	18.36	0.3627	0.9715	0.6097	0.1628
slope	HH	24.39	0.3628	0.9848	0.7305	0.1445
	LH	8.39	0	0.7832	0.4661	0.141
	LL	44.23	0	0.7832	0.4556	0.102
	HL	22.99	0.3627	0.9532	0.597	0.1652
aspect	HH	23.49	0.3627	0.9669	0.666	0.1662
	LH	26.58	0	0.7832	0.4581	0.108
	LL	26.04	0.0001	0.7832	0.4564	0.1105
	HL	23.89	0.3627	0.9834	0.6654	0.171
roughness	HH	23.58	0.3628	0.9848	0.7291	0.1463
	LH	8.06	0	0.7832	0.4635	0.1402
	LL	44.56	0	0.7832	0.4562	0.1026
	HL	23.8	0.3627	0.9532	0.6028	0.1658
relief	HH	23.61	0.3628	0.9848	0.7285	0.1467
	LH	8.08	0	0.7832	0.4627	0.1397
	LL	44.54	0	0.7832	0.4563	0.1027
	HL	23.76	0.3627	0.9532	0.6032	0.1658
shade	HH	26.4	0.3627	0.9747	0.6546	0.166
	LH	39.09	0	0.7832	0.4615	0.1042
	LL	13.53	0	0.7832	0.4452	0.1218
	HL	20.98	0.3627	0.9848	0.6796	0.1709
curvature	HH	23.2	0.3627	0.9848	0.671	0.1723
	LH	24.53	0.0001	0.7832	0.4504	0.1039
	LL	28.09	0	0.7832	0.4633	0.1133
	HL	24.18	0.3627	0.9843	0.6606	0.1649

logical and topographic context. Figure 4(c) illustrates the spatial distribution of local  $R^2$  values from the GWR model for plagioclase abundance, revealing pronounced spatial heterogeneity. High  $R^2$  values ( $>0.6$ ) are concentrated along the crater rim and central peak, whereas lower values dominate the smoother crater floor, indicating significant spatial variability in model performance across geomorphic settings. This spatial variation reflects differences in the statistical relationship between plagioclase abundance and topographic parameters across different geomorphic units. At the crater rim and central peak, pronounced structural relief and exposure of fresh or shallow bedrock result in a stronger association between mineral composition and topographic gradients. This pattern is consistent with the geological contrast between Pre-Nectarian highland units, including the crater rim and central peak, and the younger basaltic infill within the crater interior of the SPA basin<sup>[34]</sup>. In contrast,

low-relief interior regions may be influenced by regolith deposition, material redistribution, and other processes<sup>[35]</sup>, so spatial variations in plagioclase abundance are affected by multiple factors, reducing the explanatory power of the regression model.

Figure 4(d) depicts the spatial variation of standardized GWR coefficients. Positive coefficients are primarily distributed along the northwestern rim and southern steep slopes, while weaker or negative coefficients prevail within the interior plains, reflecting spatial variability in both the strength and direction of mineral – topography coupling. Figure 4(e) presents the geologic unit map, providing a framework for interpreting these variations. The spatial correspondence between areas of high coefficient values and highland units and adjacent crater ejecta is consistent with the differential exposure of plagioclase-rich crustal materials associated with impact excavation and ejecta emplacement across geologic units of different ages. This spatial pattern may reflect impact-related ejecta emplacement, differential deposition, and subsequent gravitational redistribution.

In the Pre-Nectarian unit (Figure 4(f)), curvature and elevation exhibit a strong negative correlation, suggesting the preservation of remnants of ancient highlands, where deep plagioclase-enriched layers have been exposed and retained despite long-term erosion. In the Nectarian units, regression coefficients for slope and relief are predominantly positive, indicating relatively higher plagioclase abundance associated with areas of greater relief and steeper slopes. This pattern may reflect processes of uplift, impact excavation, erosion, and subsequent material redistribution following early impact structures. In contrast, within Eratosthenian volcanic lava-covered regions<sup>[36]</sup>, regression coefficients for topographic parameters are generally smaller, indicating weaker statistical relationships between plagioclase abundance and topographic gradients, likely due to the masking effect of lava flows on pre-existing mineral – topography correlations. Collectively, these unit-specific statistical patterns record the progressive modification and overprinting of the original crustal composition through the sequence of basin formation, impact cratering, and volcanic resurfacing that characterizes lunar evolution in the SPA region<sup>[37]</sup>.

## 2.4 Validation of Mineral Spectral Retrieval

Based on Kaguya MI multispectral imagery, the Plagioclase Spectral Index (PSI) was introduced to indicate the relative enrichment of plagioclase in lunar highland studies. PSI is defined as the reflectance ratio  $R_{750}/R_{950}$ , reflecting the spectral feature of plagioclase, which exhibits lower reflectance near 950 nm compared with 750 nm<sup>[38]</sup>. It should be noted that PSI is calculated from a single-band ratio and primarily reflects the spectral response of plagioclase, whereas the plagioclase abundance data used in this study are retrieved from multispectral information through spectral endmember unmixing. Therefore, PSI serves here as an independent spectral proxy related to mineral abundance, providing auxiliary information for analyzing the spatial relation-

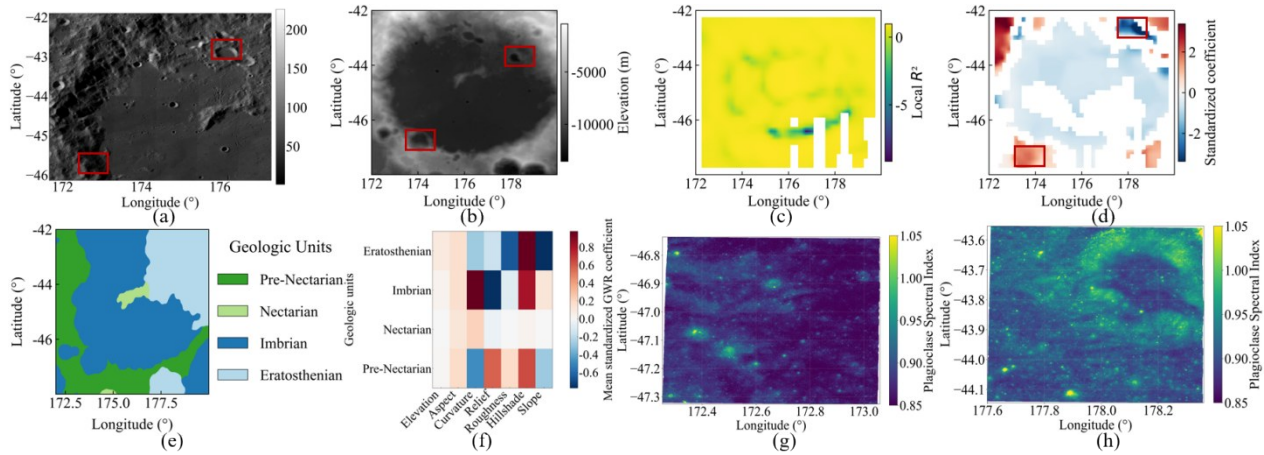


Fig. 4 Comprehensive remote sensing and geological statistical analysis results of the Von Kármán Crater: (a) WAC image; (b) DEM; (c) Spatial distribution of local regression fitting accuracy (Local  $R^2$ ) for plagioclase abundance; (d) Spatial variation of standardized Geographically Weighted Regression (GWR) coefficients; (e) Geologic unit map; (f) Heatmap of mean standardized GWR coefficients for topographic factors in different geologic units; (g) Spatial distribution details of plagioclase spectral index in the northern red-boxed sub-region and (h) spatial distribution details in the southern red-boxed sub-region

图4 冯·卡门撞击坑综合遥感与地质统计分析结果: (a)宽角相机(WAC)影像; (b)数字高程模型(DEM)影像; (c)斜长石丰度局域回归拟合精度空间分布; (d)标准化地理加权回归(GWR)系数空间变化特征; (e)地质单元分布图; (f)不同地质单元内地形因子的平均标准化 GWR 系数热力图; (g)北部红色框选子区斜长石光谱指数空间分布细节; (h)南部红色框选子区斜长石光谱指数空间分布细节

ship between minerals and topographic parameters.

To validate the plausibility of the mineral - topography relationships revealed by the GWR model from a spectral perspective, areas of positive and negative significant spatial clustering identified using the  $G_i^*$  statistic were selected for comparison. Mean PSI values and their distributions within these clusters were analyzed to assess spectral response differences.

Figures 4(g) and 4(h) present detailed spatial distributions of the plagioclase spectral index (PSI) within the northern and southern subregions highlighted in Figure 4(a) and Figure 4(b) plagioclase abundance to topography is small. In the negatively significant low-value clustering region (the northern boxed area in Figure 5(d)), the regression coefficients linking plagioclase abundance to topography exhibit relatively low magnitudes. This pattern is primarily attributed to post-impact surface modification and space weathering, both of which weaken the original coupling between topography and composition, thereby reducing the statistical response of mineral distributions to topographic gradients<sup>[39-40]</sup>.

The observed local discrepancies between PSI and GWR coefficients, particularly in zones affected by secondary impacts, highlight the complexity of surface processes that can decouple spectral signatures from immediate topographic influences. Nevertheless, their overall spatial correspondence underscores a regionally coherent relationship between plagioclase abundance and topography. This consistency, validated through independent methodological approaches using both the spectral index and spatial regression, strengthens the interpretation of the regional correspondence between plagioclase distribution and geomorphic features.

### 3 Discussions

We combined SELENE/Kaguya Multiband Imager (MI) visible - near infrared reflectance data with Lunar Reconnaissance Orbiter (LRO) digital elevation models to map plagioclase abundances and quantify their spatial relationships with slope, relief, and elevation across two contrasting lunar terrains, the Von Kármán crater and the Mare Crisium Basin. Geographically weighted regression and bivariate spatial correlation analyses demonstrate that mineral - topography relationships are spatially non-stationary across these distinct geological settings. In Von Kármán, plagioclase concentrations are associated with steep slopes and structural highs, whereas in Mare Crisium, they correlate primarily with elevation. These contrasting patterns suggest potential differences in underlying geological processes and provide a basis for the following discussion.

The results indicate clear spatial non-stationarity in plagioclase - topography relationships across different geological units. In Von Kármán crater, plagioclase abundance is more strongly associated with slope and local relief, with higher values concentrated along the crater rim and central peak regions, whereas in Mare Crisium Basin the relationship with elevation is more evident. This contrast likely reflects the combined effects of impact excavation, volcanic infilling, and differences in crustal composition, suggesting that mineral - topography coupling on the Moon is strongly dependent on geological setting.

Several limitations should be acknowledged. Bivariate Moran's I and GWR are effective for identifying spatial association and local non-stationarity, but the results may be influenced by bandwidth selection and multicollinearity among topographic parameters. Therefore, the

observed relationships are best interpreted as spatial patterns that may reflect geological processes, rather than as direct evidence of causal links. Moreover, the analysis is limited to two representative regions and mainly to plagioclase abundance, which may restrict the broader applicability of the results to other lunar terrains. The current study underutilizes lunar surface spectral information, and future work will integrate hyperspectral analysis techniques, adapted from spatial - spectral feature extraction methods originally developed for satellite-borne aircraft contrail detection<sup>[41]</sup>, to enhance the detection of fine-scale mineralogical heterogeneity on the lunar surface. Future work should incorporate higher-resolution and multi-source datasets, extend the framework to additional minerals and geological settings, and further evaluate the robustness of the observed spatial relationships using independent compositional constraints from future lunar missions.

## 4 Conclusions

This study presents a framework for analyzing the spatial relationships between mineral abundances and topographic parameters using lunar visible to near-infrared remote sensing-derived mineral data and digital elevation models (DEM). Representative geological units including Von Kármán crater and Mare Crisium Basin were systematically investigated.

The spatial relationships between mineral abundances and topography exhibit pronounced heterogeneity and spatial clustering across the studied lunar units. Bivariate Moran's  $I$  analysis indicates a significant positive association between plagioclase abundance and slope in the Von Kármán crater (Moran's  $I = 0.32$ ,  $p < 0.01$ ), and between plagioclase abundance and elevation in the Mare Crisium Basin (Moran's  $I = 0.28$ ,  $p < 0.01$ ). Local spatial clustering further resolves these associations. In the Von Kármán crater, high - high (HH) clusters of plagioclase abundance with slope account for 31.89% of the study area, with a mean abundance of 0.6493. Although HH proportions for other topographic factors range from 18.96% to 34.04%, these relationships are not statistically significant and are therefore not considered further. In the Mare Crisium Basin, HH clusters associated with elevation occupy 29.02% of the area, with a mean abundance of 0.7011.

Geographically weighted regression (GWR) analysis indicates spatial variability in the strength of mineral-topography associations. Adjusted  $R^2$  values for GWR models range from 0.32 to 0.67, exceeding those of global regression models. Steep slopes and central peak regions exhibit higher local  $R^2$  values ( $>0.6$ ), whereas flatter basins and lava-covered areas exhibit lower local  $R^2$  values ( $<0.3$ ). Standardized regression coefficients between elevation and plagioclase abundance in the Von Kármán crater range from -0.23 to 0.71, with maximum values concentrated in highland units and minimum values in volcanic terrains.

Comparison of plagioclase spectral index (PSI) with GWR coefficients shows that positive clusters correspond

to relatively high PSI values, while negative clusters correspond to relatively low PSI values. Positively significant clusters have mean PSI values 18 - 24% higher than negatively significant clusters, providing an independent spectral validation of mineral and topography relationships.

The integrated use of bivariate spatial autocorrelation, local clustering, and GWR provides a comprehensive quantitative approach for characterizing spatial associations between minerals and topography across impact-dominated and volcanic-flooded lunar terrains, enabling systematic assessment of mineral distribution patterns and evaluation of potential landing sites, while also offering new insights into lunar surface processes and practical guidance for future exploration planning and landing site selection.

## References

- [1] Zhang Z G, Zhang L, Du T R, et al. Petrography and mineralogy of lunar magnesian anorthositic meteorite Northwest Africa 8599[J]. *Geological Journal of China Universities*, 2025, 31(3): 286-300.  
(张真光, 张浪, 杜天然, 等. 月球镁质斜长岩陨石 NWA 8599 的岩相学与矿物化学研究[J]. *高校地质学报*, 2025, 31(3): 286-300.
- [2] Wang Q L. Geochemical classification of lunar rocks based on multi-source data: A case study of the Mare Crisium region[J]. *Journal of Geology*, 2024, 48(4): 393-401.  
(王庆龙. 基于多源数据对月球岩石地球化学分类: 以危海地区为例[J]. *地质学刊*, 2024, 48(4): 393-401.
- [3] Deng J Y. Spatial - temporal analysis and geological evolution of the Paleolunar impact basin on the Moon[D]. Beijing: China University of Geosciences (Beijing), 2020.  
(邓佳音. 月球古月宙撞击盆地的时空演化分析[D]. 中国地质大学(北京), 2020.
- [4] Stoffler D, Ryder G, Ivanov B A, et al. Cratering history and lunar chronology[J]. *Reviews in Mineralogy and Geochemistry*, 2006, 60(1): 519-596.
- [5] Cao H J. Petrogenesis and magmatic evolution of lunar mare basalts: new constraints from lunar breccia meteorites and Chang'e-5 lunar soils[D]. Jinan: Shandong University, 2023.  
(曹海军. 月球玄武岩成因与岩浆演化: 来自月球角砾岩陨石和嫦娥五号月壤的新约束[D]. 山东大学, 2023.
- [6] Neukum G, Ivanov B A, Hartmann W K. Cratering Records in the Inner Solar System in Relation to the Lunar Reference System[J]. *Space Science Reviews*, 2001, 96(1): 55-86.
- [7] Crawford I A. Lunar Resources: A Review[J]. *Progress in Physical Geography*, 2014, 39(2): 137-167.
- [8] Liu J G, Zhang S, Ouyang Z Y, et al. The key scientific and technological issues in lunar resource exploration [J]. *China Mining*, 2025, 34(1): 1-8.  
(刘建忠, 张圣, 欧阳自远, 等. 月球资源勘查的关键科学与技术问题[J]. *中国矿业*, 2025, 34(01): 1-8.
- [9] Zhao Z, Yang Y, Guo D, et al. Variations in lunar regolith mineralogy along the Chang'e-4 Yutu-2 traverse: combined effects of ejecta sedimentation and subsequent modification [J]. *Science China Earth Sciences*, 2025, 55(7): 2344-2358.  
(赵振兴, 杨亚洲, 郭弟均, 等. 嫦娥四号-玉兔二号巡视路径月壤矿物成分变化: 溅射物沉积和后期改造的共同作用[J]. *中国科学: 地球科学*, 2025, 55(7): 2344-2358.

- [10] Zhou Y, Zhao H, Che M, et al. Automatic detection of lunar craters based on DEM data with the terrain analysis method[J]. *Planetary and Space Science*, 2018, 160: 1-11.
- [11] Xiao Z Y, Yue Z, Xie M, et al. Impact history of the Moon and its modification of lunar surface materials[J]. *Bulletin of Mineralogy, Petrology and Geochemistry*, 2023, 42: 462 - 477.
- [12] Li C, Li Y, Pang R H, et al. Impact-induced ultra-high melting point oldhamite discovered in Chang' E-6 lunar soil[J]. *Nature Communications*, 2025, 16(1): 2155.
- [13] Hapke B. Space weathering from Mercury to the asteroid belt [J]. *Journal of Geophysical Research: Planets*, 2001, 106 (E5): 10039 - 10073.
- [14] Hiesinger H, Jaumann R, Neukum G, et al. Ages of mare basalts on the lunar nearside[J]. *Journal of Geophysical Research: Planets*, 2000, 105(E12): 29239-29275.
- [15] Head J W, Wilson L. Lunar mare volcanism: Stratigraphy, eruption conditions, and the evolution of secondary crusts[J]. *Geochimica Et Cosmochimica Acta*, 1992, 56(6): 2155-2175.
- [16] Wilson L, Head J W. Lunar Gruithuisen and Mairan domes: Rheology and mode of emplacement[J]. *Journal of Geophysical Research Planets*, 2003, 108(E2).
- [17] Thiessen F, Besse S, Staid M I, et al. Mapping lunar mare basalt units in mare Imbrium as observed with the Moon Mineralogy Mapper (M<sup>3</sup>) [J]. *Planetary and Space Science*, 2014, 104: 244-252.
- [18] Hayne P O, Greenhagen B T, Foote M C, et al. Diviner Lunar Radiometer Observations of the LCROSS Impact[J]. *Science*, 2010, 330(6003):477-479.
- [19] Pieters C, Shkuratov Y, Kaydash V, et al. Lunar soil characterization consortium analyses: Pyroxene and maturity estimates derived from Clementine image data[J]. *Icarus*, 2006, 184(1): 83-101.
- [20] Pieters C M, Noble S K. Space Weathering on Airless Bodies [J]. *The Journal of Geophysical Research Planets*, 2016, 121 (10): 1865-1884.
- [21] Hiesinger H, Head J W, Wolf U, et al. Ages and stratigraphy of mare basalts in Oceanus Procellarum, Mare Nubium, Mare Cognitum, and Mare Insularum[J]. *Journal of Geophysical Research: Planets*, 2003, 108(E7).
- [22] Liu J J, Liu B, Ren X, et al. Evidence of water on the lunar surface from Chang' E-5 in-situ spectra and returned samples [J]. *Nature Communications*, 2022, 13(1): 3119.
- [23] Feng Y J, Tang P L, Tong X H, et al. Mineral Impact on Brightness Temperature of the Moon: A Bivariate and GWR Approach With Microwave Radiometer Data[J]. *IEEE Transactions on Geoscience and Remote Sensing*, 2025, 63: 4503118.
- [24] Pieters C, Shkuratov Y, Kaydash V, et al. Lunar soil characterization consortium analyses: Pyroxene and maturity estimates derived from Clementine image data[J]. *Icarus*, 2006, 184(1): 83-101.
- [25] Green R O, Pieters C, Mouroulis P, et al. The Moon Mineralogy Mapper (M<sup>3</sup>) imaging spectrometer for lunar science: Instrument description, calibration, on-orbit measurements, science data calibration and on-orbit validation[J]. *Journal of Geophysical Research: Planets*, 2011, 116(E10).
- [26] Ohtake M, Pieters C M, Isaacson P, et al. One Moon, many measurements 3: Spectral reflectance [J]. *Icarus*, 2013, 226 (1): 364-374.
- [27] Lemelin M, Lucey P G, Miljković K, et al. The compositions of the lunar crust and upper mantle: Spectral analysis of the inner rings of lunar impact basins [J]. *Planetary and Space Science*, 2019, 165: 230-243.
- [28] Wang Q L. Geochemical classification of lunar rocks based on multi-source data: A case study of the Mare Crisium region [J]. *Journal of Geology*, 2024, 48(4): 393-401. (王庆龙. 基于多源数据对月球岩石地球化学分类:以危海地区为例[J]. *地质学刊*), 2024, 48(04): 393-401.
- [29] Li F, Wu B, Yang M, et al. Topographic and occlusion analysis of the Chang'e-4 landing site in the Von Kármán crater [J]. *Scientia Sinica Technologica*, 2019, 49(12): 1385-1396. (李飞, 吴波, 杨眉, 等. 嫦娥四号冯·卡门撞击坑着陆区地形及月面遮挡分析[J]. *中国科学: 技术科学*), 2019, 49(12): 1385-1396.
- [30] Di K C, Zhu M H, Yue Z, et al. Topographic evolution of Von Kármán crater revealed by the lunar rover Yutu-2[J]. *Geophysical Research Letters*, 2019, 46(22): 12764-12770.
- [31] McBratney A B, Webster R, Burgess T M. The design of optimal sampling schemes for local estimation and mapping of regionalized variables—I [J]. *Computers & Geosciences*, 1981, 7 (4): 331-334.
- [32] Anselin L. Local Indicators of Spatial Association—LISA [J]. *Geographical Analysis*, 1995, 27(2): 93-115.
- [33] Porter J R. Identifying spatio-temporal patterns of articulated criminal offending: An application using phenomenologically meaningful police jurisdictional geographies [J]. *Systems Research & Behavioral Science*, 2011, 28(3): 197-211.
- [34] Wilhelms D E, Oberbeck V R, Aggarwal H R, et al. Size-frequency distributions of primary and secondary lunar impact craters [J]. *Lunar and Planetary Science Conference Proceedings*, 1978, 9: 3735-3762.
- [35] Yuan Z F. Research on lunar basalt period classification and mineral components analysis methods with microwave remote sensing [D]. Beijing University of Technology, 2024. (袁子峰. 月球微波遥感玄武岩期次分类与矿物成分分析方法研究 [D]. 北京工业大学, 2024.
- [36] Huang J, Xiao Z, Flahaut J, et al. Geological characteristics of Von Kármán crater, northwestern South Pole - Aitken Basin: Chang' E-4 landing site region [J]. *Journal of Geophysical Research: Planets*, 2018, 123(7): 1684-1700.
- [37] Marchi S, Bottke W F, Kring D A, et al. The onset of the lunar cataclysm as recorded in its ancient crater populations [J]. *Earth and Planetary Science Letters*, 2012, 325: 27-38.
- [38] Ling Z, Qiao L, Liu C, et al. Composition, mineralogy and chronology of mare basalts and non-mare materials in Von Kármán crater: Landing site of the Chang'E4 mission [J]. *Planetary and Space Science*, 2019, 179: 104741.
- [39] Ohtake M, Matsunaga T, Haruyama J, et al. The global distribution of pure anorthosite on the Moon [J]. *Nature*, 2009, 461 (7261): 236-240.
- [40] Hemingway D J, Garrick-Bethell I, Kreslavsky M A, et al. Latitudinal variation in spectral properties of the lunar maria and implications for space weathering [J]. *Icarus*, 2015, 261: 66-79.
- [41] Xie S X, Li P F, Zhao S W, et al. Aircraft contrail detection based on satellite-borne hyperspectral images [J]. *Journal of Infrared and Millimeter Waves*, 2026, 45(1): 182-194. (谢书馨, 李鹏飞, 赵思维, 等. 基于星载高光谱图像的飞行器尾迹检测 [J]. *红外与毫米波学报*), 2026, 45(1): 182-194.

## 基于可见 - 近红外遥感的月表矿物丰度与地形参数的

## 空间耦合研究

焦雷蕾<sup>1</sup>, 徐聿升<sup>1,2</sup>, 黄荣<sup>1,2</sup>, 刘世杰<sup>1,2\*</sup>, 唐盼丽<sup>1,2</sup>, 王超<sup>1,2</sup>, 冯永玖<sup>1,2</sup>, 童小华<sup>1,2</sup>

(1. 同济大学 同济大学测绘与地理信息学院, 上海 20092;

2. 同济大学 上海市航天测绘遥感与空间探测重点实验室, 上海 20092)

**摘要:**月表矿物的空间分布格局记录了岩浆活动、物质分异及后期撞击改造等关键地质过程,是认识月球演化历史的重要遥感信息基础。本文基于 SELENE(Kaguya)多波段成像仪(Multiband Imager, MI)可见—近红外(415–950 nm)矿物丰度反演产品,结合数字高程模型(DEM)提取的地形参数,构建统一空间尺度的定量分析框架,以研究月海单元内主要矿物相的空间分布及其与地貌特征的关系。选取冯·卡门撞击坑和危海盆地等具有代表性的月球大型撞击构造与月海盆地为研究区,定量刻画近红外敏感矿物丰度与地貌特征在不同地质单元中的空间关联特征。矿物丰度与地形参数在区域尺度上呈现显著的空间集聚特征,且在不同地质背景与构造单元中表现出明显的空间非平稳性,反映了岩浆活动、后续撞击改造及其与古地形协同响应等多过程长期作用的结果,为基于遥感数据的月球表面地质解译与演化历史分析提供了定量依据。

**关键词:**月球矿物;地貌特征;双变量空间自相关;地理加权回归模型

中图分类号:P207

文献标识码:A